Observations of Atmospheric Structure and Dynamics in the Owens Valley of California with a Ground-Based, Eye-Safe, Scanning Aerosol Lidar*

STEPHAN F. J. DE WEKKER

University of Virginia, Charlottesville, Virginia

SHANE D. MAYOR+

National Center for Atmospheric Research,# Boulder, Colorado

(Manuscript received 7 May 2008, in final form 18 December 2008)

ABSTRACT

First results are presented from the deployment of the NCAR Raman-Shifted Eye-Safe Aerosol Lidar (REAL) in the Owens Valley of California during the Terrain-Induced Rotor Experiment (T-REX) in March and April 2006. REAL operated in range–height indicator (RHI) and plan position indicator (PPI) scanning modes to observe the vertical and horizontal structures of the aerosol and cloud distribution in a broad valley in the lee of a tall mountain range. The scans produce two-dimensional cross sections that when animated produce time-lapse visualizations of the microscale and mesoscale atmospheric structures and dynamics. The 2-month dataset includes a wide variety of interesting atmospheric phenomena. When the synoptic-scale flow is strong and westerly, the lidar data reveal mountain-induced waves, hydraulic jumps, and rotorlike circulations that lift aerosols to altitudes of more than 2 km above the valley. Shear instabilities occasionally leading to breaking waves were observed in cloud and aerosol layers under high wind conditions. In quiescent conditions, the data show multiple aerosol layers, upslope flows, and drainage flows interacting with valley flows. The results demonstrate that a rapidly scanning, eye-safe, ground-based aerosol lidar can be used to observe important features of clear-air atmospheric flows and can contribute to an improved understanding of mountain-induced meteorological phenomena. The research community is encouraged to use the dataset in support of their observational analysis and modeling efforts.

1. Introduction

Observations of atmospheric flow over complex terrain remain a research priority for several reasons. First, observations are needed to evaluate numerical simulations that are challenged by terrain because of the difficulty of accurately representing subgrid-scale processes and boundary conditions. Flow over terrain induces flow separation (Jiang et al. 2007), rotors (Doyle and Durran 2002, 2007), turbulence, and mountain waves (Smith et al. 2007) at a variety of temporal and spatial scales. Second, flow over complex terrain can pose a hazard to aircraft. Third, complex terrain is also capable of inducing circulations that vent particulate matter and trace gasses into midtroposphere altitudes and the free atmosphere (Henne et al. 2004). As a result, complex terrain flows may have a significant role in air quality and potentially in climate change studies.

Great technological advancements have occurred in the past 40 years with laser remote sensing that have proven very useful in the understanding of atmospheric dynamics and structure. Shortly after the development of the first pulsed lasers, the applicability of lidar to the study of mountain-wave-related phenomena was recognized. Collis et al. (1968) were the first to document aerosol lidar observations in the Sierra Nevada in

* Supplemental information related to this paper is available at the Journals Online Web site: http://dx.doi.org/10.1175/2009JAMC2034.s1.

+ Current affiliation: College of Natural Sciences, California State University, Chico, California.

The National Center for Atmospheric Research is sponsored by the National Science Foundation.

Corresponding author address: Stephan F. J. De Wekker, Dept. of Environmental Sciences, University of Virginia, P.O. Box 400123, Charlottesville, VA 22904-4123.
E-mail: dewekker@virginia.edu

DOI: 10.1175/2009JAMC2034.1

February and March 1967, followed by more comprehensive observations by Viezee et al. (1973) in March and April 1969 and 1970. These studies provided evidence that pulsed lasers could be used to locate clouds and aerosols and study atmospheric dynamics.

As laser and optical technology matured in the 1970s and 1980s, Doppler lidars were used to study flow over complex terrain (Banta et al. 1990, 1999; Blumen and Hart 1988). Doppler lidars enabled direct measurement of the radial wind velocity field and, because of the relatively long wavelength and sufficiently low energy density in the beam, featured eye safety. During this time, the development and application of shorter-wavelength aerosol backscatter lidars expanded. However, ground-based scanning aerosol lidar observations of atmospheric structure and flow in mountainous terrain ceased. One reason for this may be the hazard associated with pointing a non-eye-safe laser beam at various elevations and azimuth angles. This is especially true for scanning lidars operating in terrain where the beam might intersect the ground, resulting in an eye injury.

The advent of the Raman-Shifted Eye-Safe Aerosol Lidar (REAL; Mayor and Spuler 2004; Spuler and Mayor 2005) in recent years has made it possible to safely apply the ground-based scanning aerosol lidar technique in mountainous terrain and near research aircraft. The Terrain-Induced Rotor Experiment (T-REX) in March and April 2006 provided an ideal opportunity to demonstrate this application. REAL was deployed to observe mountain waves, rotors, and boundary layer structures in the absence of rotors. This paper presents a selection of some of the atmospheric features observed by REAL. The objective is to document the capability and usefulness of an eye-safe scanning elastic backscatter lidar in mountainous terrain. In future papers, more detailed and comprehensive analyses will be presented by combining the lidar observations with surface and airborne data, and atmospheric numerical models. An example of such an analysis is provided by Doyle et al. (2009). Lidar data will also be used to evaluate high-resolution numerical simulations of flow in complex terrain as demonstrated, for example, in Mayor et al. (2003), and De Wekker et al. (2004).

The organization of this paper is as follows: section 2 briefly describes the T-REX field campaign including the location of REAL. Section 3 provides background on the REAL with emphasis on what characteristics make it unique. Section 4 provides descriptions of eight mountain-induced atmospheric phenomena occurring in disturbed and quiescent conditions. Challenges associated with the field deployment of REAL are described in the appendix. Time-lapse animations of the lidar data observations from many of the cases are available online as part of the supplemental material for this article as indicated in the title-page footnote.

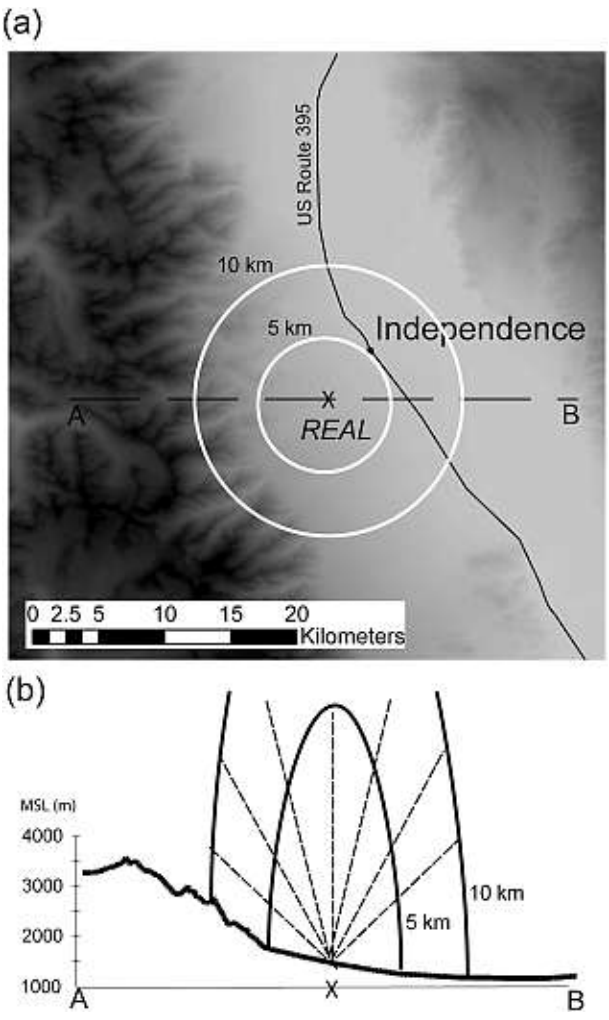

FIG. 1. (a) Topography of the Owens Valley around Independence, CA, and (b) horizontal cross section of topography on a west–east line through the location of REAL. The location of REAL is indicated with the × in (a) and (b). Lidar range gates at 5 and 10 km are depicted with the white lines in (a) and the black lines in (b).

2. Field experiment

T-REX took place in March and April 2006 near Independence, California, in the Owens Valley in the lee of the Sierra Nevada (Fig. 1). In this location, the Sierra Nevada is the tallest, steepest, quasi-two-dimensional topographic barrier in the contiguous United States with several peaks above 4 km, including the highest peak in the lower 48 states (Mount Whitney, 4418 m). The White-Inyo range with peaks around 3 km forms the eastern wall of the Owens Valley. The Owens Valley is

FIG. 2. The NCAR REAL as deployed at T-REX in the Owens Valley. This photograph was taken looking toward the west.

approximately 150 km long and 15–30 km wide. The average elevation change between the Sierra Nevada crest and the valley floor is roughly 3000 m. The Owens Lake region in southeastern California, a prominent example of dust source amplification by anthropogenic disturbance, is considered one of the largest sources of fine particulate matter (particles having diameters smaller than 2.5 μm, PM2.5) in the Western Hemisphere (Gill and Gillette 1991). Given the complex topography of the region, plumes can be vented to 2 km AGL, transported 250 km, and cover 90 000 km^2 (Reid et al. 1994). The period from October through April typically includes the largest and most frequent duststorms (Cahill et al. 1996).

The objective of T-REX was to study the interaction and coupling between atmospheric rotors, mountain waves, and boundary layer dynamics. Detailed information on the field study and the observation systems that were deployed can be found in Grubišić et al. (2008). T-REX was designed to document a coupled system of large vertical extent, reaching from the ground to the upper troposphere and lower stratosphere. For this reason, the field campaign had both substantial ground-based and airborne components. The ground-based instrumentation was also used for observing the structure and evolution of the valley boundary layer in the absence of rotors. The site for REAL was positioned on the western side of the Owens Valley on an alluvial slope at 1413 m MSL (36°46′10.65″N, 118°13′52.42″W; see Fig. 2). This location placed the lidar within range of several other ground-based observing systems and featured an unobstructed view of the atmosphere in all directions.

3. Instrument

REAL (Mayor and Spuler 2004; Spuler and Mayor 2005) was developed by the National Center for Atmospheric Research (NCAR) to provide a high-performance, ground-based, scanning, and eye-safe aerosol lidar to the community that would be useful in a broad variety of atmospheric science field campaigns. Deployment to T-REX was its first National Science Foundation (NSF) funded field experiment. As such, it was largely a prototype designed for experimental work and not continuous or unattended operation. Deployment in T-REX was very valuable because, in addition to collecting new visualizations of the atmospheric structure and dynamics in the Owens Valley, many insights were gained about instrument stability and performance. The ''lessons learned'' have since been used to dramatically improve the instrument's performance and reliability for future field work.

REAL was, and remains at the time of this writing, unique in that it operates at 1.5-μm wavelength with high pulse energy. Operation at this near-infrared wavelength offers maximum eye-safety, thereby enabling the safe transmission of energetic laser pulses. Laser radiation at this wavelength is invisible. These characteristics make it possible to operate REAL in populated areas or near aircraft, without human spotters or safety radars.

REAL is a direct analog detection lidar. This type is quite different from the 2-μm-wavelength heterodyne Doppler lidars (Henderson et al. 1991; Grund et al. 2001) that were also deployed during T-REX (Grubišić

et al. 2008). Heterodyne Doppler lidars are designed and optimized to sense the frequency shift of coherent backscattered radiation. Such a design is an ideal solution for sensing radial velocity, but it places limitations on the resolution and usefulness of the aerosol backscatter imagery. REAL, on the other hand, is optimized to be an eye-safe scanning aerosol lidar that does not sense the Doppler frequency shift. The absence of system requirements for heterodyne detection allows REAL to obtain higher-resolution aerosol data than presently available commercial Doppler lidar systems.

Because REAL transmits energetic laser pulses, the backscatter signal is usually detectable to a range of several kilometers from a single laser pulse. This feature enables it to scan rapidly without the need to integrate the backscatter signal from multiple laser pulses. When the laser transmitter is optimized, it is capable of producing approximately 170 mJ of pulse energy at 10 Hz. This performance was achieved at the beginning of the field experiment. Unfortunately, the pulse energy steadily decreased during the 2-month deployment due to the slow increase of beam divergence of an untested commercial Nd:YAG pump laser used as part of the lidar transmitter. This resulted in lower energy density in the wavelength-converting Raman cell and reduced conversion efficiency. As a result, the data quality from the beginning of the experiment is much better than the data from the end of the experiment. Additional hardware problems that were encountered during deployment of REAL at T-REX are described in the appendix.

4. Results

The lidar images and animations presented in the following subsections and in the supplemental information show the spatial structure and temporal evolution of the atmosphere as revealed by the variability of the aerosol backscatter intensity. Many factors, such as particle concentration, particle size distribution, and extinction, influence the aerosol backscatter intensity. To confirm that the primary cause of the backscatter variability used to reveal flow features results from changes in particle concentrations, we installed an in situ aerosol particle counter on a tower within the line of sight from the lidar. The resulting data are the only ground-based measurements of aerosol particle concentration from the field campaign. The Met One model 9012 particle counter sampled air at a rate of approximately $4.7 \times 10^{-5}\ \mathrm{m^3\ s^{-1}}$. During the experiment the number of particles was counted in the following six size ranges: 0.3–0.5, 0.3–1.0, 0.3–2.5, 0.3–7.0, and 0.3–10 μm at a rate of 1 Hz. The particle counter collected data almost continuously from 16 March to 14 April 2006 on a meteorological tower at a height of 5 m AGL. The tower was located at a range of 1950 m and 234.4° azimuth from the lidar site. Between approximately 2252 and 2330 UTC on 27 March 2006, the lidar beam was directed and held stationary toward a location near the tower. The lidar backscatter data from the range nearest the location of the meteorological tower are compared with the number of particles between 0.3 and 10 μm in Fig. 3. Both the particle counter and lidar data are plotted at 1-s intervals while the solid lines represent a 10-s running average. The data indicate that the changes in lidar backscatter intensity observed over short periods (minutes) are predominantly caused by changes in the particle number concentration. During this period, the relative humidity was approximately constant at 25%. While the in situ particle number concentration measurements presented here are just one of several causes of aerosol backscatter variability, they confirm that changes in concentration of medium- and large-sized aerosol particles have a significant impact on the lidar backscatter signal. The comparison with lidar data also highlights the synergy of using eye-safe scanning aerosol backscatter lidars and in situ particle sensors simultaneously for a more comprehensive understanding of the aerosol distribution and characteristics.

The lidar images and animations presented in the following subsections demonstrate the value of a scanning elastic backscatter lidar in studies of flow in mountainous terrain. The cases are presented in sequential order. For a summary of the cases, see Table 1.

a. 28 February 2006: Mountain-wave activity

Figure 4 is a popular scene associated with mountain-wave activity in the lee of the Sierra Nevada range. This photograph was captured by an aircraft pilot (R. Symons) on 5 March 1950. It provides a powerful perspective of the atmospheric flow (from right to left) and a flow visualization made possible only by the presence of clouds, dust, and smoke. Without sophisticated active remote sensors, this photograph provided observational confirmation of the existence of mountain-induced atmospheric hydraulic jumps (Turner 1973; Lighthill 1967). The photograph falls short, however, on the delivery of three critical types of information that the lidar can provide. First, the photograph can only provide relative distance information. The lidar, as an active sensor, can provide extremely accurate, three-dimensional location and range information. Second, the lidar by virtue of its scanning ability and its ability to operate over long periods can provide frames at a sufficient rate and duration to make time-lapse animations. Third, the lidar can elucidate the structure of the

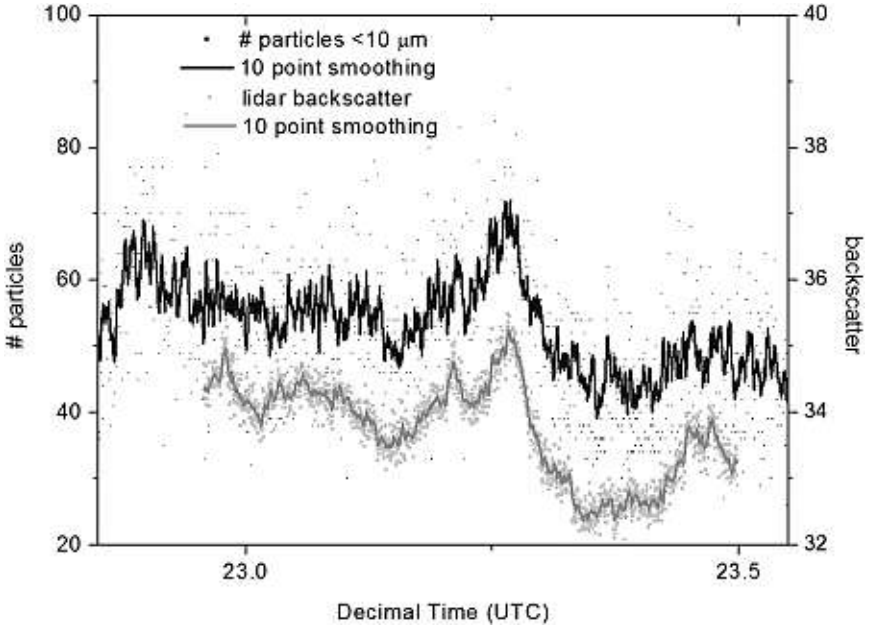

FIG. 3. Comparison of 10-Hz lidar backscatter intensity (bottom trace) at a range of 1950 m and the number of particles (top trace) in the range 0.3–10 μm measured at 1 Hz at a height of 5 m between approximately 2252 and 2330 UTC 27 Mar 2006. The solid lines are running averages over 10 s.

visually clear air and sunlight is not required to illuminate the scene. In addition, the lidar is sensitive to the presence of and variations in, aerosol optical depth far below the ability of humans to perceive. Therefore, the lidar images are capable of revealing structures in regions that would appear clear in a photograph.

As a first example, Fig. 5 is a single vertical (range–height indicator, RHI) scan at 2315 UTC 28 February 2006, revealing a flow pattern that is likely similar to that shown in Fig. 4. Blue shading represents relatively clean air while red shading represents cloudy or aerosol-laden air. The white shading denotes areas where the backscatter or the signal-to-noise ratio was low. The location of the lidar is at 0 km and the scan is directed toward 250° azimuth. This means that the left side of the figure is approximately west. At an azimuth angle of 250°, hard target returns from the terrain of the eastern slopes of the Sierra Nevada at about 7 km range can be observed at altitudes of 1 km higher than the altitude of the lidar site. At altitudes less than 1 km above terrain level, clouds are observed advecting over the mountain range. As the cloud structures advect down the slope, the optical backscattering intensity is reduced, suggesting evaporation. The spatial and temporal variability of the backscatter in this region indicates that the cloud is inhomogeneous and turbulent. The time-lapse animation of this flow reveals this descending cloud and the aerosol backscatter layer that remains confined to altitudes of 1 km or less above the terrain. At a distance of 3–4 km west of the lidar, the flow abruptly diverges in the vertical, and turbulent elements increase their depth by as much as 1500 m in 2 km. It appears that some of these plumes have their roots near the surface, suggesting that they may be composed of mineral dust and

TABLE 1. Summary of the cases presented in this paper.

Date (2006)	Case	Fig.
28 Feb	Mountain-wave activity	5
3–4 Mar	Transition from undisturbed to disturbed conditions (IOP1)	6, 7
4 Mar	Multilayer aerosol structure	8, 9
9 Mar	Mountain-wave structure (IOP3)	10
11–12 Mar	Collision of drainage and valley flows	11, 12
23 Mar	Upslope flow	13
26 Mar	Windstorm (IOP6)	14, 15
16–17 Apr	Shear instability billows (IOP13)	16, 17

FIG. 4. Photograph of a downslope windstorm in the Owens Valley of CA during March 1950. (Photo taken by R. Symons.)

organic material raised from the surface. (The animation of this event is available online as an electronic supplement.) The lidar is sufficiently powerful to also reveal an optically thin, elevated aerosol layer (indicated by the curved black line in Fig. 5) that traces the mountain wave above the turbulent boundary layer in the leeside of the Sierra Nevada. From the animation of the lidar scans, the mountain wave is estimated to have an amplitude of about 1 km and a horizontal wavelength of about 10 km. The animation also shows that the wave is initially stationary and subsequently propagating to

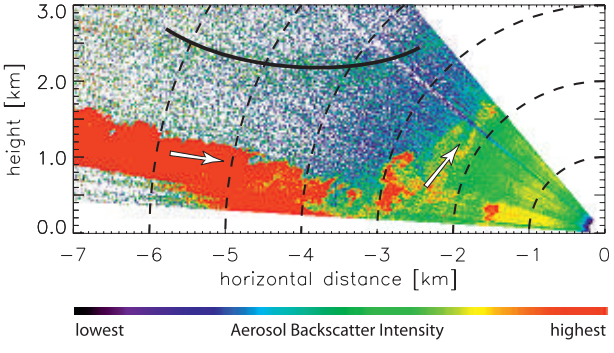

FIG. 5. A single RHI scan from REAL at 2315 UTC 28 Feb. Animation of this sequence shows downslope flow and mountain-wave activity. The curved black line was superimposed to point out an optically thin aerosol layer that traces a mountain wave. Range rings are shown every 1 km.

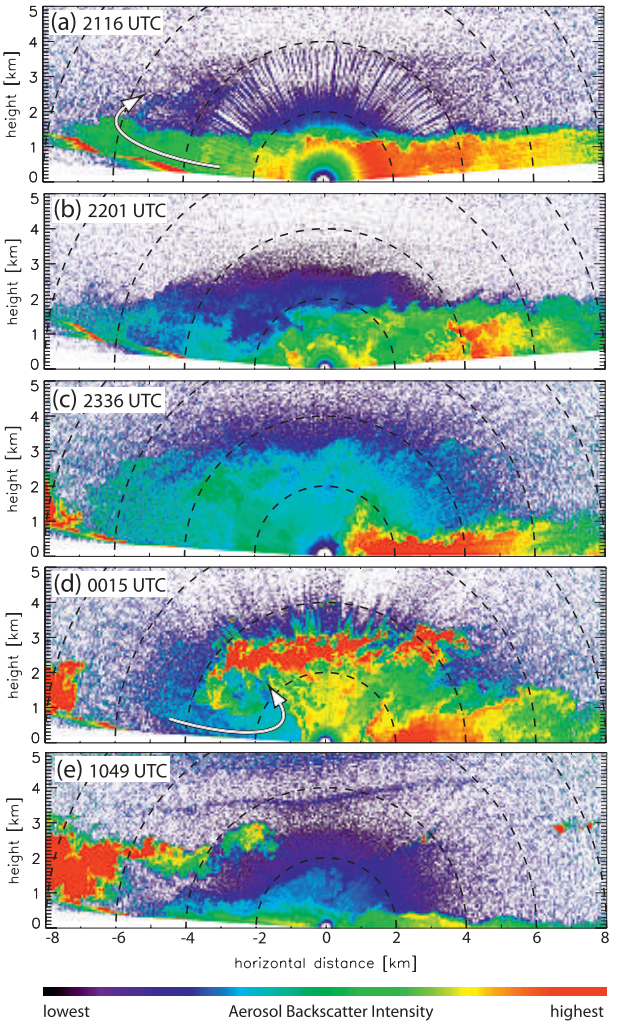

FIG. 6. RHI scans obtained by REAL during the IOP on 2 Mar 2006 at (a) 2116, (b) 2201, and (c) 2336, and on 3 March 2006 at (d) 0015 and (e) 1049 UTC. The azimuth angle of the scan is 250° for (a) and (b), and 281.9° for (c)–(e). Cold-color shading represents clean air while warm-color shading represents aerosol-laden air. The arrow in (a) indicates easterly flow up the Sierra Nevada slopes. The arrow in (d) indicates westerly flow down the Sierra Nevada slopes. This relatively clean air from the west undercuts the aerosol-laden southeasterly flow in Owens Valley. Range rings are drawn every 2 km.

the east while increasing in amplitude and decreasing in length. The backscatter intensity of the elevated aerosol layer is much less than that of the turbulent boundary layer. However, this optically thin layer is sufficiently coherent over time that its presence and movement are noticeable in the animation. The synoptic flow at this time was from the west and in excess of 40 m s^{-1} at 5000 m MSL, where a strong increase in potential temperature was noted. Such a situation is conducive to the formation of mountain waves (e.g., Whiteman 2000).

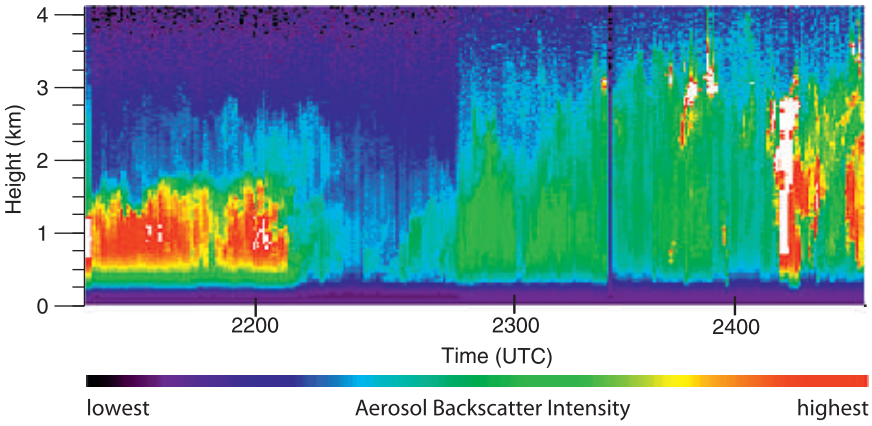

FIG. 7. Time-vs-altitude image of aerosol backscatter created by selecting the zenith profiles of RHI scans between 2130 UTC 2 Mar and 0030 UTC 3 Mar 2006. The image was created to demonstrate the difficulty of interpreting boundary layer aerosol structure from a vertically pointing lidar during disturbed conditions.

b. 3 March 2006: Transition from undisturbed to disturbed conditions (IOP 1)

The first intensive observational period of T-REX took place from 0000 UTC 2 March to 1500 UTC 3 March [for a list of the intensive observing periods (IOPs), see Grubišić et al. (2008)]. Lidar images and the animation from this time period (see the supplement to this article for the animation of this time period) reveal a variety of interesting phenomena ranging from a quiescent convective boundary layer early in the IOP to a disturbed boundary layer near the end. A sequence of lidar images during the IOP is shown in Fig. 6. As before, blue and white shadings represent relatively clean air while nonwhite colors represent various levels of aerosol-laden air. The top panel in Fig. 6 shows the aerosol structure in a convective boundary layer at around 2200 UTC. The aerosol layer extends from the surface to approximately 2 km AGL, corresponding approximately with the top of the convective boundary layer from a sounding in the center of the valley at about 2300 UTC. Southerly up-valley flows and upslope flows were observed during this period. Between 2100 and 2130 UTC, a dust cloud approaching from the south was observed by the lidar operator and this corresponds with the area of enhanced backscatter that is visible east of the lidar at 2116 and 2201 UTC (Figs. 6a and 6b, respectively). The animation corresponding to the times in Fig. 6 shows the movement of the area of enhanced backscatter up the slope (indicated by the black arrow in panel a) and there is an indication that the vertical transport and mixing of aerosol is enhanced by the upslope flows.

At around 2330 UTC (Fig. 6c), lidar animations revealed a sudden transition from upslope- to downslope-directed flows. Clouds that spill over the Sierra Nevada from the west are now visible (similar to Fig. 5). The air that flows down the east side of the Sierra Nevada slopes is relatively clean and undercuts the aerosol-laden air in the Owens Valley (Fig. 6d). The aerosol-laden air from the Owens Valley has an easterly component and converges with the flow down the Sierra Nevada slopes. The convergence area is visible in the lidar data, as are the resulting circulations with aerosols transported upward and then horizontally and downward (Fig. 6d). The animation shows that a rapid-scanning aerosol lidar is capable of revealing both radial and tangential components of aerosol structure motion, whereas a Doppler lidar provides highly accurate measurements of the radial velocity. Characteristics of the flow and boundary layer structure on multiple scales can clearly be identified in an animation of the lidar images around this time. The circulation on the eastern side of the convergence area may indicate the presence of a rotorlike circulation but this must be confirmed or rejected by examining additional observations.

Ground-based, stationary, vertically pointing lidars have been used in many studies to monitor the aerosol-layer depth (e.g., Cohn et al. 1998). We can simulate this technique using REAL data by selecting the zenith-pointing profiles from the RHI scans and plotting them as time–height images (Fig. 7). It is clear that the boundary layer structure changes significantly at approximately 2210 UTC, but an explanation of the flow characteristics cannot be given with only vertical-pointing lidar data. By comparing scans (Fig. 6) with the image resulting from the subset of vertical beams (Fig. 7) during the period of

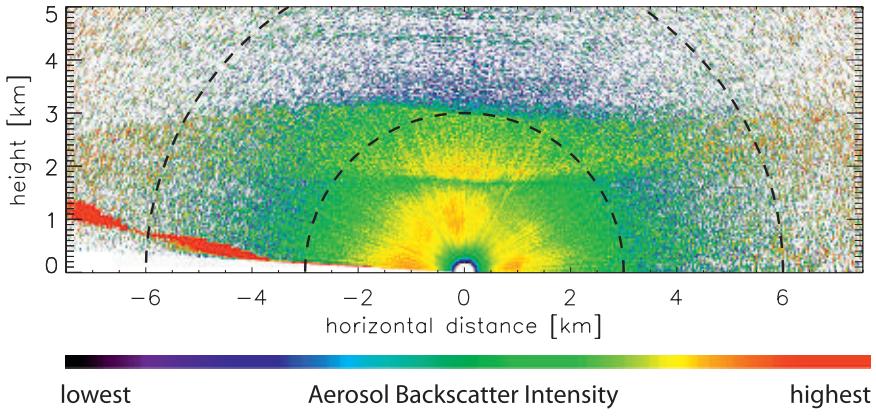

FIG. 8. RHI scan at 2200 UTC 4 Mar 2006. Azimuth angle is 250° (left of origin) and 70° (right of origin). Range rings are shown every 3 km.

transition to disturbed conditions, one can conclude that much more insight on the structure and motion of the lower atmosphere can be gained by scanning.

c. 4 March: Multilayer aerosol structure

The weather conditions in the morning and afternoon of 4 March were characterized by few clouds and weak winds, a situation in which a convective boundary layer is expected to develop well. From a single RHI scan at 2200 UTC (Fig. 8), a two-layer aerosol structure is visible with the bottom layer reaching almost 2000 m AGL and the top or elevated layer reaching about 3000 m AGL. The thickness of the elevated layer is not horizontally homogeneous with deeper aerosol layer thicknesses in the center of the valley than near the base and over the slopes. Such a structure of aerosol layers has also been observed in other field studies (De Wekker 2008) and is thought to be associated with thermally driven upslope flows and compensating sinking motions away from the slope. Elevated layers such as the one observed in this event are thought to be present frequently in complex-terrain areas (McKendry and Lundgren 2000) but because of a lack of observations, their structures and dynamics have not been studied very well. During T-REX, it was often found that an elevated aerosol layer served as tracers of wave motion, providing important insight into mountain-wave characteristics. The thermodynamic structure of the atmosphere near the time of the vertical scan in Fig. 8 is shown in Fig. 9. Evident is the convective boundary layer

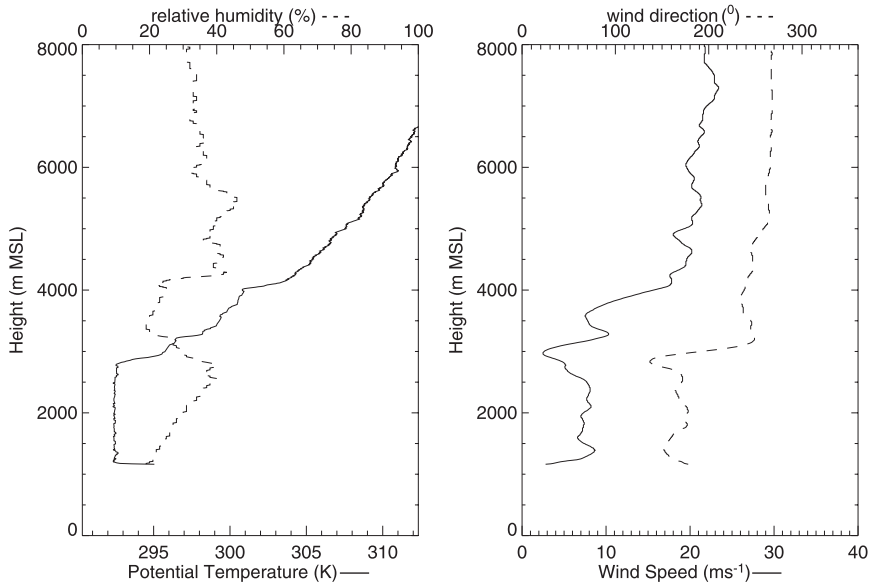

FIG. 9. Vertical profiles of (left) potential temperature and relative humidity and (right) wind speed and direction at 2308 UTC 4 Mar 2006.

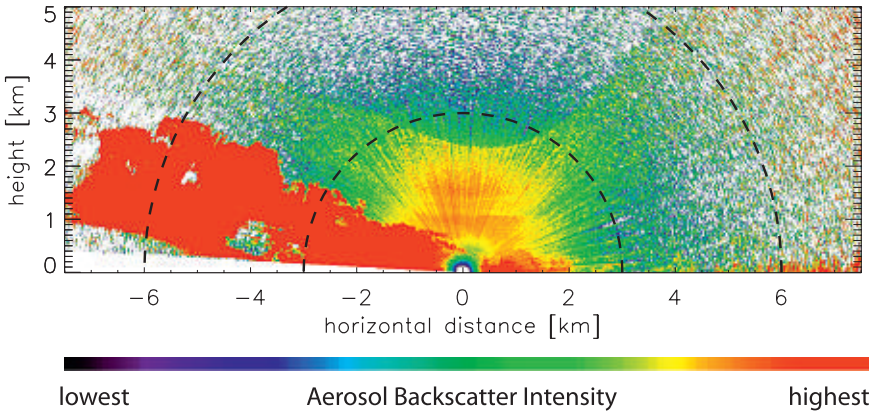

FIG. 10. RHI scan at 2130 UTC 9 Mar 2006. Azimuth angle is 250° (left of origin) and 70° (right of origin). Range rings are shown every 3 km.

extending from the surface to a strong inversion at 2800 m MSL or about 1700 m above the lidar site. Moderately strong upvalley (southerly) flows of 5–10 m s^{-1} and strong westerly flows dominate in and above the convective boundary layer, respectively. At about 4000 m MSL, or 2900 m AGL, a second strong inversion can be identified. The elevated inversions at 1700 and 2900 m AGL approximately correspond with the tops of the two aerosol layers in Fig. 8.

d. 9 March 2006: Mountain-wave structure (IOP 3)

As was indicated in the previous section, elevated aerosol layers that are not in contact with the surface of the earth can serve as tracers of wave motion. On 9 March, during IOP 3, the lidar captured images of an optically thin aerosol layer that descended into the Owens Valley. The layer is faint but can be identified in individual RHI scans, such as shown in Fig. 10 for 2130 UTC. As in many of the cases discussed in this paper, the layer and the wave that it traces out are more discernible in the animation (see the online supplement to this article to access the animation) due to their coherence over time. The layer is located between roughly 2500 and 4000 m AGL within several kilometers on either side of the lidar site. The time-lapse animation of this situation shows the location of the trough of the wave changing over time with an amplitude that increases to almost 2000 m by 2130 UTC. The ascending branch of the wave changes its slope over time also. Finally, toward the end of the animation near 2300 UTC, clouds from over the Sierra Nevada range descend into the valley and obscure the aerosol layer. While the lidar data can describe some important characteristics of this mountain-wave event, a more comprehensive case study should be conducted by employing the other forms of observations and attempting to simulate this event with a numerical model.

e. 11–12 March 2006: Collision of drainage and valley flows

The following case provides detailed observations of the interaction of downslope flow colliding and mixing with along-valley flow on the evening and night of 11–12 March 2006. Visualization is made possible by the two air masses having significantly different levels of aerosol backscattering. Along-valley flow has a predominantly southerly or northerly component and, in this case, exhibits strong aerosol backscattering intensity. This is indicated by the green, yellow, and orange colors in Fig. 11. The downslope flow has a predominantly westerly component and has significantly lower backscatter intensity (white and blue colors) than the along-valley flow. The sharp red edge along the left edge of each panel indicates the location where the lidar beam intersects the terrain.

This case begins while the lidar was collecting full 360° azimuth PPI scans. The lidar operator noticed a large horizontal gradient of aerosol backscattering 2 km northwest of the lidar site (see Figs. 11a and 11b, and also visit the online supplement to see the animation). The air mass to the south and east of the boundary zone exhibited high backscattering intensity and PPI scan animations reveal that this valley air was advancing from the south-southwest. The lidar operator changed the lidar scanning at approximately 0250 UTC to collect vertical cross sections oriented along a 140°–320° azimuth transect (Fig. 12). The series of RHI scans reveals that the air mass with strong aerosol backscatter intensity extends from the surface to approximately 500–750 m above the altitude of the lidar site (Fig. 12; visit the online supplement to see the animation). This layer becomes abruptly shallower northwest of the lidar site and vanishes at distances beyond approximately 2 km. Figure 12b provides an expanded view of the boundary between the two

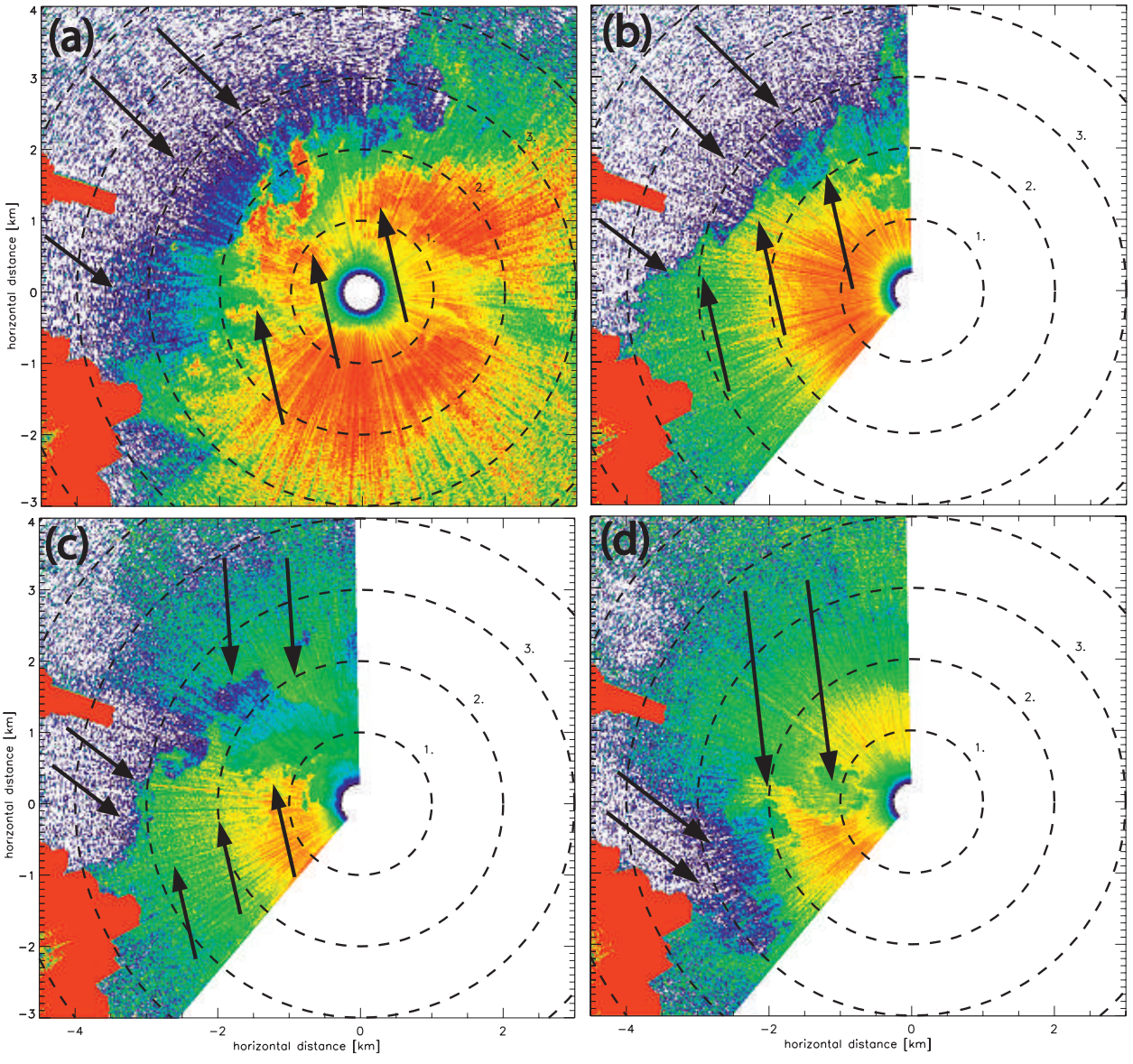

FIG. 11. PPI scans collected with a 4° elevation angle at (a) 0243, (b) 0400, (c) 0424, and (d) 0431 UTC 12 Mar 2006. Range rings are shown every 1 km. In (a) and (b), a boundary revealed by a sharp gradient in backscatter lies to the NW of the lidar site. In (c), an air mass with moderate intensity optical scattering (green shades) emerges from the north. In (d), the northerly flow dominates the valley and the slope flow is trapped along the foothills. The arrows indicate the direction of the flow derived from the corresponding animation.

air masses. Animations of the RHI and PPI scans clearly reveal the dynamics of the mixing along this boundary zone. Wisps of high optical scattering air at the boundary are lifted from near the surface to hundreds of meters altitude while being quickly transported eastward.

Later in the evening, valley flow from the north with strong optical backscatter intensity sweeps across the lidar's observing area. Figure 11c shows the arrival of this air mass at 0424 UTC. At this time, the downslope flow air mass appears to be confined between the two valley air masses. The northerly down-valley flow eventually dominates the valley and by 0431 UTC all perturbations in aerosol structure are moving to the south (Fig. 11d). PPI scans reveal pulses of low optical scattering downslope air confined to a narrow region along the foothills west of the lidar site. (Visit the online supplement to this paper to see the conclusion of this event.) This dramatic event took place during an evening that the lidar operator would have otherwise described as calm and uneventful.

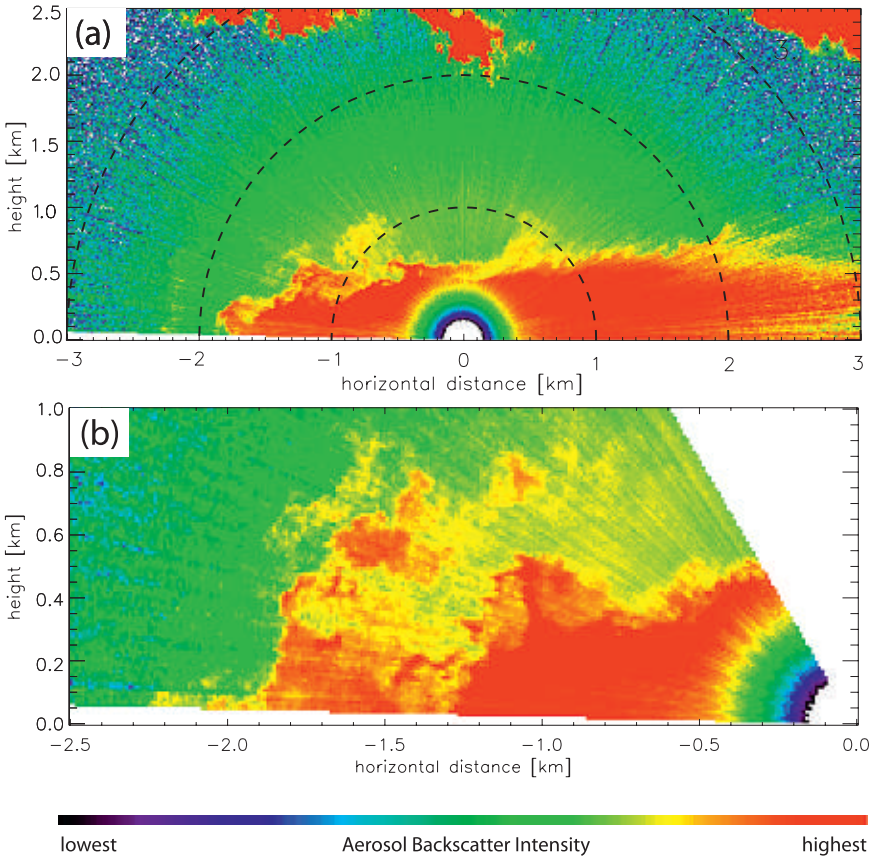

FIG. 12. RHI scans along a transect oriented from 320° azimuth (left of origin) to 140° azimuth (right of origin) at (a) 0251 and (b) 0302 UTC 12 Mar 2006. Note the different horizontal and vertical axes in (a) and (b). Range rings are shown every 1 km in (a).

f. 23 March 2006: Upslope flow

Vertical profiles of horizontal wind speed over sloped terrain are difficult to obtain at high temporal and spatial resolutions using in situ instruments. The following case provides an example of the potential power of aerosol lidar measurements in the investigation of slope flows. Slope flows are thermally driven flows that are directed down the slope at night and up the slope during the daytime (e.g., Whiteman 2000). Downslope flows have been observed in past studies using atmospheric tracers (e.g., Gudiksen et al. 1984). Upslope flows, however, tend to be more difficult to see because vertical mixing acts to disperse the smoke rapidly and below visible concentrations. During T-REX, we found that dust raised by vehicles driving on an unpaved road west of the lidar site provided a tracer for upslope and downslope flows. An example of RHI scans showing the movement of the dust plume is shown in Fig. 13. The scans are 1–2 min apart and show a more rapid upslope transport of dust in the layer just above the surface rather than aloft. The upslope flows could potentially play an important role in the formation of elevated aerosol layers as seen, for example, in Fig. 8. The ability of the lidar to track aerosol plumes provides an opportunity to study these poorly observed flows. In future experiments, tracers could be released to create plumes that would be tracked using a scanning lidar. Profiles of the wind speed could then be obtained using the correlation technique (Mayor and Eloranta 2001).

g. 26 March 2006: Windstorm (IOP 6)

The most dramatic weather event of T-REX occurred near the end of IOP 6 on 25 March. Anemometers on a tower located to the west of the lidar site recorded peak wind speeds as high as 42.2 m s^{-1} at 5 m AGL and 47 m s^{-1} at 30 m AGL during this event. Damage was reported in the city of Independence, California. During the most intense period of this event, the westerly winds were so severe that the lidar operators did not point the lidar to the west due to the possibility of flying debris damaging the glass beam-steering unit window.

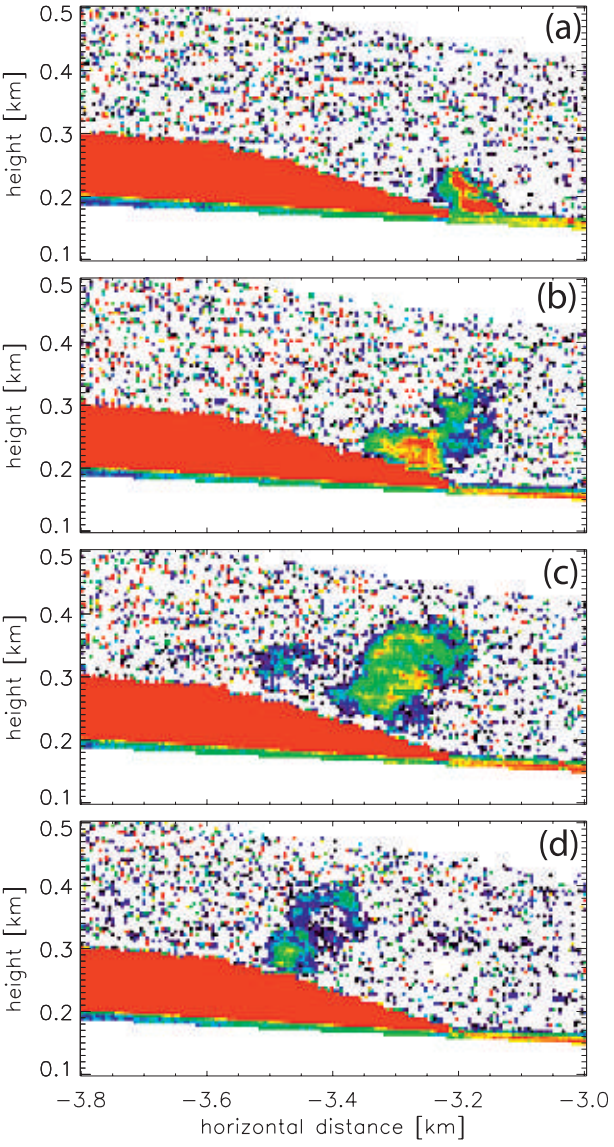

FIG. 13. RHI scans directed toward 245° azimuth at (a) 1616:42, (b) 1619:11, (c), 1620:22, and (d) 1622:26 UTC 23 Mar.

Animations of lidar scans reveal a deep clear layer, nearly transparent to the lidar, descending into the valley. (Visit the online supplement to this article to see the animation of RHI scans.) A wave cloud is observed at altitudes above 7 km AGL and as high as 10 km AGL. From the animations, the amplitude of the wave is estimated to be about 2 km and the wavelength 20 km. A single RHI scan form the animation is shown in Fig. 14. The spatial details of the turbulent flow that leads into the large aerosol cloud located to the east of the lidar site are noteworthy. (Visit the online supplement to see the animation of the PPI scan.) Wind-parallel surface-layer streaks are produced in both numerical simulations and tank experiments (e.g., Drobinski and Foster 2003, Lin et al. 1996). However, they are difficult to observe in the real atmosphere. At a range of about 2 km downstream of the lidar site, approximately nine streaks can be identified in PPI scans (Fig. 15). The streaks are each approximately 200 m wide, are spaced every 500–1000 m apart, and terminate into the dust cloud. Given the slope of the valley floor and the elevation of the beam, the altitude of the scan plane is about 100 m at 2 km downstream (east) of the lidar site. South of the lidar, where the beam approaches the terrain, finer-scale streaks are observed. These streaks are each about 50 m wide and are spaced about 250 m apart. (A PPI animation of the conclusion of the event can be viewed as part of the online supplement to this paper.) This mountain-wave case provides another example that demonstrates the usefulness of aerosol lidar data for the investigation of flow and turbulence in complex terrain.

h. 16–17 April 2006: Shear instability billows (IOP 13)

This case documents the evolution and characteristics of shear instability billows on an elevated aerosol layer between approximately 0100 and 0200 UTC on 17 April 2006. Figure 16 shows a sequence of three RHI scans over approximately 2 min. The top of the aerosol layer is very evident in the aerosol backscatter data. The eastward propagation of the perturbations on this interface in time-lapse animations from the same time period can also easily be identified. (See the supplement to access the animation.) The slope of the backscatter layer steepens and overturns in certain areas while it propagates to the east. The flow visualization is suggestive of forward shear and is consistent with Doppler lidar observations (Doyle et al. 2008). From Fig. 16, it can be derived that the vertical and horizontal scales of the billows are approximately 1000 and 3000 m, respectively. To quantify the characteristics of the billows in a more objective way, a Hovmöller diagram was constructed. To do this, we selected a sequence of RHI scans across the valley between 0100 and 0200 UTC and plotted the backscatter intensity averaged between 2400 and 2500 m of altitude as a function of horizontal distance and time in Fig. 17. The nearly linear light-shaded segments from the upper-left to the lower-right parts of Fig. 17 indicate the eastward propagation of the billows. The segments extend from about −2000 m to +2000 m in approximately 6 min, corresponding with a phase velocity of about 11 m s^{-1}. The regularity in wave velocity and wavelength over the period of 1 h is apparent. This case study shows that quantitative information about features in aerosol lidar data can be derived using Hovmöller diagrams.

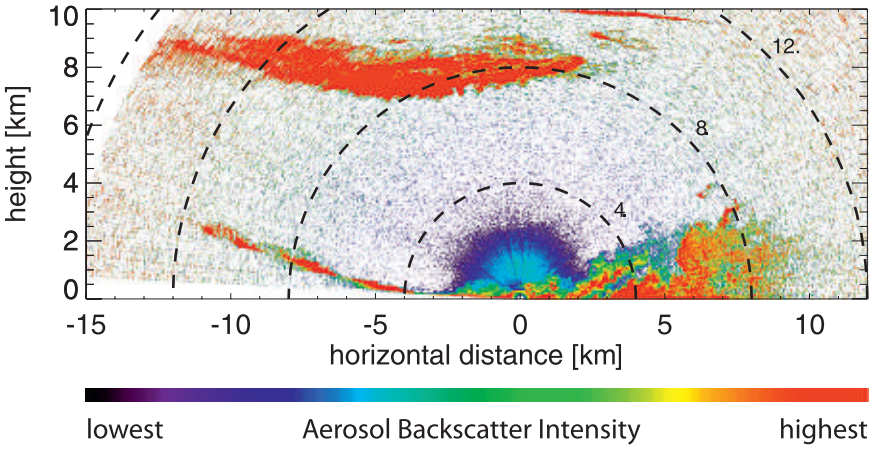

FIG. 14. RHI scan collected at 0315 UTC 26 Mar along a transect running from 250° azimuth (left of origin) to 70° azimuth (right of origin). Range rings are shown every 4 km.

5. Conclusions

Deployment of the NCAR REAL in T-REX was useful in several ways. First, it demonstrated the recently developed ability to perform traditional backscatter lidar measurements with good performance, scanning, and eye safety. The scan speed and sensitivity to aerosols are sufficient to provide time-lapse animations of the clear air using aerosols as a tracer of the atmospheric structure and motion. The resulting imagery possesses clear advantages over aerosol lidars that are restricted to pointing vertically and the data also complement scanning Doppler lidar observations by providing both radial and tangential components of the motion of macroscopic aerosol structures. Second, several hardware design flaws were identified. These have since been corrected and have resulted in improved field reliability and performance. Most important, however, deployment of REAL at T-REX provided new visualizations of atmospheric flow in a mountain-valley setting. The scanning capability of REAL combined with an appropriate location a few kilometers away from the base of the Sierra Nevada allowed for the visualization of complex flow structure.

During the 2-month operation of REAL, a variety of flows were observed. In synoptically disturbed conditions, the animations reveal rotorlike circulations of boundary layer aerosols and mountain waves from elevated aerosol layers and clouds. The positions, wavelengths, and amplitudes of the waves appeared variable whereas smaller-scale waves, such as the billows discussed in section 4h, exhibited more regularity. Clouds spilling over the Sierra Nevada were a recurring feature in the animations during westerly flow. Shear instabilities occasionally leading to breaking waves were observed in elevated cloud and aerosol layers under high wind conditions. In synoptically undisturbed (quiescent) conditions, aerosol backscatter cross sections reveal the structure of the daytime boundary layer, the presence of multiple layers in the valley atmosphere, and the interaction between valley and slope flows. Thermally driven upslope and downslope flows were documented by tracking dust plumes at the base of the Sierra Nevada. It was demonstrated that quantitative information about the flows can be extracted using a sequence of scans and Hovmöller-type diagrams. The variety of flows and boundary layer structures visualized by the lidar was not fully explained in the current paper. In future studies, we intend to perform an in-depth investigation of several of the cases presented here using additional analyses and observations from other instruments. We also intend to use the lidar data to evaluate the performance of mesoscale models and particle dispersion models over mountainous terrain.

We have shown that a rapidly scanning ground-based aerosol lidar can significantly contribute to an improved understanding of mountain meteorological phenomena, and we encourage the research community to use the dataset in support of their observational analysis and/or modeling efforts.

Acknowledgments. The National Center for Atmospheric Research is sponsored by the National Science Foundation. Any opinions, findings, and conclusions or recommendations expressed in this publication are those of the authors and do not necessarily reflect the views of the National Science Foundation. The authors are indebted to S. M. Spuler and B. M. Morley for their roles in the development and deployment of REAL at T-REX. Thanks are given to Steve Oncley for overseeing the

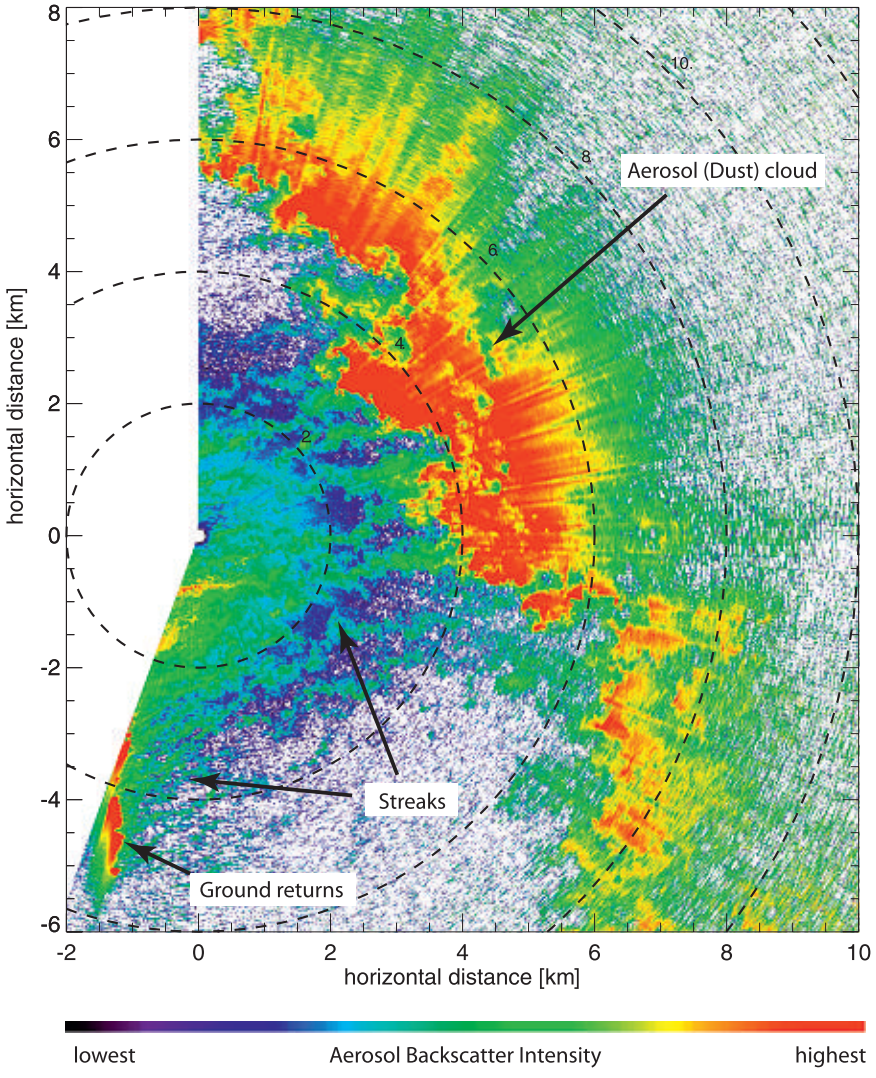

FIG. 15. A PPI scan collected at 0254 UTC 26 Mar 2006 shows surface-layer streaks terminating feeding into a large aerosol cloud east of the lidar site. The elevation angle of this scan was 3.0° above a horizontal plane. Range rings are shown every 2 km.

integration of the particle counter on the west ISFF tower; D. J. Kirshbaum, G. Poulos, and T. M. Weckwerth assisted with data collection; J. Van Andel, R. Rilling, and J. Hurst processed and archived the resulting dataset; G. Farquharson contributed IDL software to create the images. We thank V. Grubišić and J. Doyle for helpful discussions; J. Doyle suggested the use of Hovmöller-type diagrams in the lidar analysis (as presented in section 4h).

APPENDIX

Instrument Issues

Some hardware problems are briefly described here because they have an impact on the data quality and scope of the dataset. First, when in operation, the beam steering unit (BSU) allowed rainwater to leak into the laboratory beneath it, which contains electronic and optical devices. For this reason, we did not operate the lidar during precipitation events. The BSU did fail during operation occasionally and required an electrical reset to resume functioning. In addition to these problems, we found that the backscatter data exhibited an artificial near-field ''halo.'' This systematic error in the data became most apparent at low pulse energy and during low optical scattering conditions. After the experiment, engineers determined that the window of the BSU caused a reflection of the transmitted pulse to be projected back into the instrument. These photons scatter many times from reflective interior surfaces of the

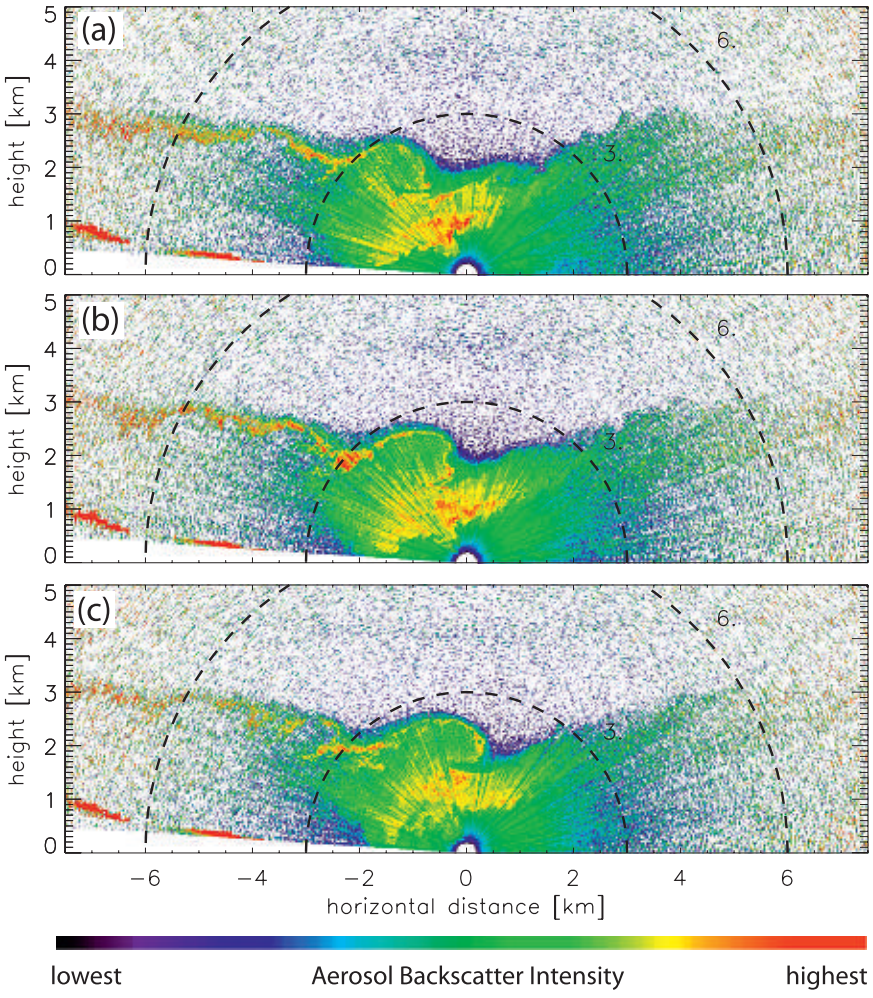

FIG. 16. RHI scans at (a) 0107:44, (b) 0108:18, and (c) 0108:52 UTC 17 Apr 2006 show progression of a shear instability billow. Range rings are shown every 3 km. The propagation speed and wavelength of these billows can be deduced from the Hovmöller diagram shown in Fig. 17, below.

BSU and the telescope, and eventually make their way into the field-of-view of the receiver. To minimize this effect, the BSU window mount was replaced with a version that holds the window at an 86° angle to the outgoing laser beam (instead of perpendicular). Flocking paper was also applied to the main reflective surfaces in the vicinity of the BSU and receiver to reduce stray light scatter.

For T-REX, REAL operated in a polarization sensitive configuration. A detailed description of this configuration can be found in Mayor et al. (2007). In summary, linearly polarized laser radiation was transmitted and a two-channel receiver recorded parallel and perpendicular components of the backscattered radiation. Total backscatter intensity is obtained by adding the parallel and perpendicular components. The depolarization ratio, obtained by dividing the perpendicular channel by the parallel channel, results in a measure of the scatterer's sphericity. However, as discussed by Mayor et al. (2007), the reflective coating of the BSU mirrors were a large source of systematic error. Therefore, the depolarization ratio data from T-REX must be used with caution. In general, these data may be useful in documenting relative changes in the depolarization ratio, but the absolute magnitude is not accurate and changes as a function of pointing angle. In the future, the BSU mirrors may be replaced with ones that have thin film coatings designed to minimize these errors.

During the T-REX experiment, the lidar was able to collect RHI scans (vertical cross sections) or PPI scans (shallow angle conic sections). Switching from one scan mode to another required an operator on site. In the majority of scans, the BSU was initially positioned to direct the laser beam a few degrees above the horizontal plane. Directing the laser beam into the terrain at short distances risked damaging the lidar receiver's

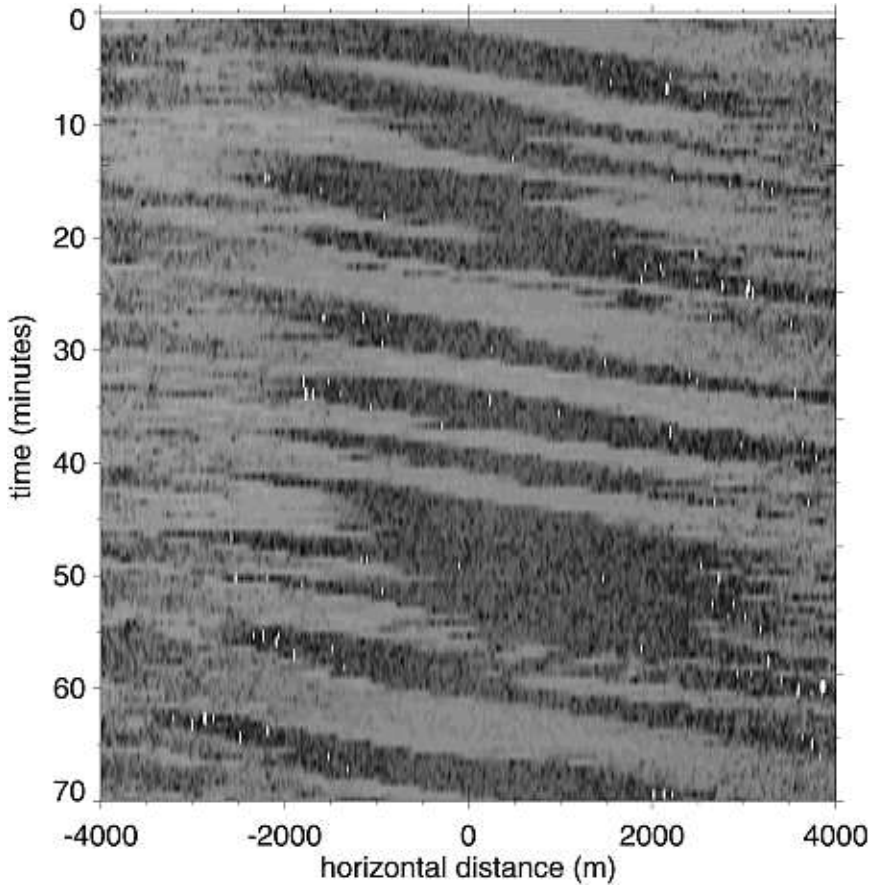

FIG. 17. Hovmöller-type diagram using mean backscatter data at a 2400–2500-m-height range between 0103 and 0213 UTC 17 Apr 2006. Lighter shades depict larger backscatter intensity values.

photodetector. The slope of the alluvial plain in the immediate vicinity of the lidar site is about 3° (sloping down to the east). Only occasionally did we scan at a slight negative elevation angle to the east in order to probe the structure of the atmosphere in the valley lower than the lidar itself. Reflections from terrain more than a few kilometers from the lidar site are not sufficiently intense to damage the photodetector.

The lidar transmitted laser pulses into the atmosphere at a rate of 10 Hz. To create image sequences with a sufficient rate to produce smooth time-lapse animations, we typically scanned at 4° or 6° s^{-1}. At a 6° scan rate, a full 180° RHI scan takes about 30 s. A full PPI requires about 1 min. Although the BSU is constructed with slip rings to allow continuous PPI scans in one rotation direction, the software required to enable this capability was not complete. Therefore, the BSU was rapidly rotated back to the initial pointing angle after each scan. For sector scans, this approach has the advantage of projecting beams into the same general location in the atmosphere on a regular cycle.

The BSU is driven by two electronic motors with angle encoders. A full revolution in either coordinate is resolved into 400 000 counts. Therefore, azimuth and elevation angles are recorded with a resolution of 0.0009°. However, this is not the accuracy or precision of the BSU. Absolute pointing of the lidar is set at the beginning of the experiment by blocking the photodetector and tracking the sun. The elevation and azimuth angle of the sun can be accurately determined based on date, time, latitude, longitude, and altitude, which are measured by a GPS device at the lidar site. Variables such as tension on drive belts, deformation of mirror adhesive, and settling of the container into the soil all affect the accuracy and precision of the beam positioning over time. In general, we have found from experience that the angular position of fixed-distance objects, such as towers, under typical atmospheric refractive conditions do not change more than about 0.025° from repeated measurements over the course of months.

The laser beam was approximately 66 mm in diameter (as measured by the 1 over e^2 points of the beam profile)

at the exit aperture of the BSU. The divergence of the laser beam was 0.12 mrad (half angle) resulting in a diameter of approximately 0.3 m at 1 km and 2.4 m at the 10-km range. The laser pulse duration was approximately 6 ns, corresponding to a length of about 1.2 m. The range resolution of the instrument was limited by the bandwidth of the analog electronics in the receiver modules amplifiers. Laboratory experiments conducted after the experiment revealed that the receiver channel bandwidths ranged from 3.4 to 4.4 MHz. These rates correspond to independent samples spaced at intervals of 34–44 m, respectively. Despite this, REAL's receiver for T-REX employed an analog-to-digital converter that recorded the backscatter intensity signal at a rate of 50 million samples per second. This resulted in an oversampled backscatter signal with data points at 3-m intervals along each beam.

REFERENCES

Banta, R. M., L. D. Olivier, and J. M. Intrieri, 1990: Doppler lidar observations of the 9 January 1989 severe downslope windstorm in Boulder, Colorado. Preprints, *Fifth Conf. on Mountain Meteorology,* Boulder, CO, Amer. Meteor. Soc, 68–69.

——, L. S. Darby, P. Kaufmann, D. H. Levinson, and C.-J. Zhu, 1999: Windflow patterns in the Grand Canyon as revealed by Doppler lidar. *J. Appl. Meteor.,* **38,** 1069–1083.

Blumen, W., and J. E. Hart, 1988: Airborne Doppler lidar wind field measurements in the lee of Mount Shasta. *J. Atmos. Sci.,* **45,** 1571–1583.

Cahill, T. A., T. E. Gill, J. S. Reid, E. A. Gearhart, and D. A. Gillette, 1996: Saltating particles, playa crusts and dust aerosols at Owens (Dry) Lake, California. *Earth Surf. Processes Landforms,* **21,** 621–639.

Cohn, S. A., S. D. Mayor, C. J. Grund, T. M. Weckwerth, and C. Senff, 1998: The Lidars in Flat Terrain (LIFT) experiment. *Bull. Amer. Meteor. Soc.,* **79,** 1329–1343.

Collis, R. T. H., F. G. Fernald, and J. Alder, 1968: Lidar observations of Sierra wave conditions. *J. Appl. Meteor.,* **7,** 227–233.

De Wekker, S. F. J., 2008: Observational and numerical evidence of depressed convective boundary layer heights near a mountain base. *J. Appl. Meteor. Climatol.,* **47,** 1017–1026.

——, D. G. Steyn, and S. Nyeki, 2004: A comparison of aerosol layer and convective boundary layer structure over a mountain range during STAAARTE '97. *Bound.-Layer Meteor.,* **113,** 249–271.

Doyle, J. D., and D. R. Durran, 2002: The dynamics of mountain-wave-induced rotors. *J. Atmos. Sci.,* **59,** 186–201.

——, and ——, 2007: Rotor and subrotor dynamics in the lee of three-dimensional terrain. *J. Atmos. Sci.,* **64,** 4202–4221.

——, V. Grubišić, W. O. J. Brown, S. F. J. De Wekker, A. Dörnbrack, Q. Jiang, S. D. Mayor, and M. Weissmann, 2008: Observations and numerical simulations of intense atmospheric subrotor vortices during T-REX. Preprints, *13th Conf. on Mountain Meteorology,* Whistler, BC, Canada, Amer. Meteor. Soc, P2.11. [Available online at http://ams.confex.com/ams/pdfpapers/141121.pdf.]

——, ——, ——, ——, ——, ——, ——, and ——, 2009: Observations and numerical simulations of subrotor vortices during T-REX. *J. Atmos. Sci.,* **66,** 1229–1249.

Drobinski, P., and R. C. Foster, 2003: On the origin of near-surface streaks in the neutrally stratified planetary boundary layer. *Bound.-Layer Meteor.,* **108,** 247–256.

Gill, T. E., and D. A. Gillette, 1991: Owens Lake: A natural laboratory for aridification, playa desiccation and desert dust. *GSA Abstracts,* **23** (5), 462.

Grubišić, V., and Coauthors, 2008: The Terrain-Induced Rotor Experiment. *Bull. Amer. Meteor. Soc.,* **89,** 1513–1533.

Grund, C. J., R. M. Banta, J. L. George, J. N. Howell, M. J. Post, R. A. Richter, and A. M. Weickman, 2001: High-resolution Doppler lidar for boundary layer and cloud research. *J. Atmos. Oceanic Technol.,* **18,** 376–393.

Gudiksen, P. H., G. J. Ferber, M. M. Fowler, W. L. Eberhard, M. A. Fosberg, and W. R. Knuth, 1984: Field studies of transport and dispersion of atmospheric tracers in nocturnal drainage flows. *Atmos. Environ.,* **18,** 713–731.

Henderson, S. W., C. P. Hale, J. R. Magee, M. J. Kavaya, and A. V. Huffaker, 1991: Eye-safe coherent laser radar system at 2.1 micron using Tm, Ho:YAG lasers. *Opt. Lett.,* **16,** 773–775.

Henne, S., and Coauthors, 2004: Quantification of topographic venting of boundary layer air to the free troposphere. *Atmos. Chem. Phys.,* **4,** 497–509.

Jiang, Q., J. D. Doyle, S. Wang, and R. B. Smith, 2007: On boundary layer separation in the lee of mesoscale topography. *J. Atmos. Sci.,* **64,** 401–420.

Lighthill, M. J., 1967: Waves in fluids. *Commun. Pure Appl. Math.,* **20,** 267–293.

Lin, C.-L., J. C. McWilliams, C.-H. Moeng, and P. P. Sullivan, 1996: Coherent structures in a neutrally stratified planetary boundary layer. *Phys. Fluids,* **8,** 2626–2639.

Mayor, S. D., and E. W. Eloranta, 2001: Two-dimensional vector wind fields from volume imaging lidar data. *J. Appl. Meteor.,* **40,** 1331–1346.

——, and S. M. Spuler, 2004: Raman-Shifted Eye-Safe Aerosol Lidar. *Appl. Opt.,* **43,** 3915–3924.

——, G. J. Tripoli, and E. W. Eloranta, 2003: Evaluating large eddy simulations using volume imaging lidar data. *Mon. Wea. Rev.,* **131,** 1428–1453.

——, S. M. Spuler, B. M. Morley, and E. Loew, 2007: Polarization lidar at 1.54-microns and observations of plumes from aerosol generators. *Opt. Eng.,* **46,** 096201, doi:10.1117/12.781902.

McKendry, I. G., and J. Lundgren, 2000: Tropospheric layering of ozone in regions of urbanised complex and/or coastal terrain—A review. *Prog. Phys. Geogr.,* **24,** 359–384.

Reid, J. S., R. G. Flocchini, T. A. Cahill, and R. S. Ruth, 1994: Local meteorological, transport, and source aerosol characteristics of late autumn Owens Lake (dry) dust storms. *Atmos. Environ.,* **28,** 1699–1706.

Smith, R. B., J. D. Doyle, Q. Jiang, and S. A. Smith, 2007: Alpine gravity waves: Lessons from MAP regarding mountain wave generation and breaking. *Quart. J. Roy. Meteor. Soc.,* **133,** 917–936.

Spuler, S. M., and S. D. Mayor, 2005: Scanning eye-safe elastic backscatter lidar at 1.54 μm. *J. Atmos. Oceanic Technol.,* **22,** 696–703.

Turner, J. S., 1973: *Buoyancy Effects in Fluids*. Cambridge University Press, 367 pp.

Viezee, W., R. T. H. Collis, and J. J. D. Lawrence, 1973: An investigation of mountain waves with lidar observations. *J. Appl. Meteor.,* **12,** 140–148.

Whiteman, C. D., 2000: *Mountain Meteorology: Fundamentals and Applications*. Oxford University Press, 355 pp.